Ceramics International 51 (2025) 42250–42261

Contents lists available at ScienceDirect

Ceramics International

journal homepage: www.elsevier.com/locate/ceramint

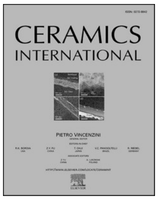
CERAMICS INTERNATIONAL

Influence of gallium doping on the thermal stability and microstructure of sintered hydroxyapatite bioceramics

Marika Sceglova [a,b], Nicola Döbelin [c], Renats Vasiljevs [a,b], Liga Stipniece [a,b,*], Janis Locs [a,b,**]

[a] *Riga Technical University Faculty of Natural Sciences and Technology, Institute of Biomaterials and Bioengineering, Paula Valdena Street 3-K1, Riga, LV-1048, Latvia*
[b] *Baltic Biomaterials Centre of Excellence, Headquarters at Riga Technical University, Riga, Latvia*
[c] *RMS Foundation, Bischmattstrasse 12, 2544, Bettlach, Switzerland*

ARTICLE INFO

Handling Editor: Dr P. Vincenzini

Keywords:
Hydroxyapatite
Gallium substitution
Sinterability
Bioceramics
Rietveld refinement

ABSTRACT

Calcium phosphates (CaPs) are extensively used in the biomedical field for bone regeneration applications. Hydroxyapatite (HAp), the main component of human bone, has been successfully used as a bone graft material. Partial calcium (Ca) substitution with gallium (Ga) can influence HAp's physicochemical properties and biological activity. In this study, Ga-doped Ca-deficient HAp (GaCDHAp) powders containing 1.6 ± 0.1 and 3.3 ± 0.4 wt% Ga were synthesized using wet chemical precipitation. Bioceramics were prepared from the synthesized GaCDHAp powders using uniaxial compaction and sintering at temperatures between 600 and 1200 °C. The quantitative phase composition and the Ga substitution in the HAp lattice were investigated by *Rietveld* refinement. It was observed that the sintering of the GaCDHAp led to the formation of biphasic CaP bioceramics composed of HAp and α-TCP. The secondary phase inhibited the densification, leading to a microporous structure of GaHAp bioceramics. Structure refinement showed that Ga substituted Ca on the Ca1 site in the HAp lattice. Charge balance was maintained by an additional partially occupied oxygen site in the structural channel.

1. Introduction

Calcium phosphate (CaP) bioceramics have been used in hard tissue reconstruction since 1980 [1]. Hydroxyapatite (HAp) is a naturally occurring CaP mineral and the main mineral component of human bone. This similarity in composition confers HAp-based biomaterials osteoconductivity, allowing integration within bone tissues. Thus, for decades, HAp-based biomaterials have been widely used for applications in bone repair, replacement, and tissue engineering [1–4]. The range of HAp-based materials is extensive and constantly expanding [5]. In the case of HAp bioceramics, numerous factors, *e.g.*, preparation and processing methods, influence their performance. Moreover, HAp has the capacity for ion exchange, and doping with different metal ions has enhanced its biological properties [6–9]. These dopants affect the physicochemical properties of HAp, which determine the possibilities of processing and application of new materials [10]. Different ions, such as magnesium (Mg), zinc (Zn), and strontium (Sr), promote the formation of secondary phases during the sintering of HAp [11–13]. The secondary phase in the form of tricalcium phosphate (TCP) can influence the biodegradability of CaP bioceramics.

Among others, due to its compelling biological properties, gallium (Ga) as a dopant has seen an increasing interest in the biomaterials field. Ga compounds are currently investigated as effective antibacterial and promising anticancer agents [14,15]. Ga^{3+} mimics iron (Fe^{3+}) in biological processes, thus disrupting iron-dependent processes in tumor cells and bacteria, leading to cell death [16,17]. In the material science field, multiple materials doped with Ga are being investigated, such as bioglass [18], CaPs [19,20], and composites [19,20]. The study focuses on Ga-containing CaPs (GaCaPs), which have shown promising results against different bacteria [21–23]. *Kurtjak* et al. studied different formulations of Ga-doped HAp (GaHAp) and revealed an antibacterial effect against *Pseudomonas aeruginosa* (*P. aeruginosa*) by the disc diffusion method [24,25]. *Pajor* et al. showed antibacterial properties of Ga and silver (Ag) functionalised HAp against *Pseudomonas fluorescens* (*P. fluorescens*) by the disc diffusion method [9]. *Shokri* et al. studied the synergy of Ga and Zn in HAp doping. By increasing the Ga concentration, they disclosed the enhanced antibacterial properties of Ga-doped or Zn- and Ga-co-doped HAp (ZnGaHAp). The results show reduced

---

* Corresponding author. Riga Technical University Faculty of Natural Sciences and Technology, Institute of Biomaterials and Bioengineering, Paula Valdena Street 3-K1, Riga, LV-1048, Latvia.
** Corresponding author. Baltic Biomaterials Centre of Excellence, Headquarters at Riga Technical University, Riga, Latvia.
E-mail addresses: liga.stipniece@rtu.lv (L. Stipniece), janis.locs@rtu.lv (J. Locs).

https://doi.org/10.1016/j.ceramint.2025.06.440
Received 23 April 2025; Received in revised form 27 June 2025; Accepted 28 June 2025

cell viability of *S. aureus* from 48 % to 6 % and *E. coli* from 57 % to 18 %. Additionally, by increasing the concentration of Ga, the viability of human mesenchymal stem cells (hMSCs) decreased compared to that of undoped HAp; however, it retained cell viability above 70 % [26]. GaCaP used as a coating for MgCa alloy reduced degradation of the alloy and promoted the formation of new bone in sheep cranial defects [27]. *Ngoc Huu* et al. introduced a multifunctional biomaterial sintered at 1200 °C, where the HAp pellets were covered with liquid Ga and Ag nanoparticles or their combination. *In vivo* findings indicate a significant reduction of bacterial growth in the presence of HAp-Ag-GaNPs in the infected cranial defects model [28].

The studies available in the literature on Ga doping mainly focus on low-crystallinity (heat-treatment temperature does not exceed 100 °C) HAp synthesized by various methods [9,22,23,26,29–32]. It has generally been observed that GaHAp has a characteristic hexagonal structure and a decrease in crystallinity with increasing Ga concentration [9,22, 23,26,29–32]. *Mellier* et al. studied Ga^{3+} influence on β-TCP ceramic obtained at 1000 °C and observed a reduction in unit cell volume with increasing Ga^{3+} concentration [21]. However, there is a shortage of information on the effect of Ga^{3+} on the high-temperature behavior of HAp (heat-processed above 600 °C). In this study, systematic and complex analyses of coherence between Ga substitution and sintering temperature of the HAp bioceramics were performed for the first time.

In our previous study, we evaluated the effect of Ga on the physicochemical and biological characteristics of HAp nanoparticles (low crystalline). The GaHAp with 2–8 wt% of Ga showed bacteriostatic properties against *P. aeruginosa* and *S. aureus*. However, when the Ga was above 4 wt%, the GaHAp showed a significant decrease in fibroblast cell viability on day 7 [29]. Accordingly, the optimal doping level of Ga was 2–4 wt%, which was used for doping the GaHAp bioceramics in this study. Insight into how Ga alters crystallinity and structural characteristics during sintering is crucial to expand the possibilities of using the GaHAp in developing new biomaterials. For the first time, the in-depth justification and the substitution behavior of Ga in the HAp crystal lattice were explored to gain deeper insights into the properties of GaHAp bioceramics.

2. Materials and methods

2.1. Synthesis of Ga-doped HAp powders

Ga-doped HAp (GaHAp) powders were synthesized using wet chemical precipitation from calcium oxide (CaO, >98 %, *Jost Chemical*, USA), orthophosphoric acid (H_3PO_4, 75 %, *Latvijas kimija Ltd.*, Latvia), and gallium nitrate hydrate ($Ga(NO_3)_3 \cdot xH_2O$, 99.9 % trace metal, *Sigma-Aldrich*, USA) as described in Ref. [29]. To calculate the required amount of $Ga(NO_3)_3 \cdot xH_2O$, the number of water molecules was determined using an inductively coupled plasma mass spectrometry (ICP-MS, *Agilent 7700X*, USA). Thus, the $Ga(NO_3)_3 \cdot 9.95H_2O$ was used as a source of Ga^{3+} ions.

Synthesis was performed in the *IKA EUROSTAR Power Control-Visc P7* (*Ika-Werke,* Germany) synthesis reactor equipped with an anchor stirrer, following the procedure below. First, the starting suspension, 0.44M $Ca(OH)_2$, was prepared by dispersing CaO in the deionized H_2O (Eq. (1)):

$$CaO + H_2O \rightarrow Ca(OH)_2 \tag{1}$$

The starting suspension was heated to 45 °C and this temperature was maintained using a laboratory hot plate with an external temperature probe. Second, the $Ga(NO_3)_3 \cdot 9.95H_2O$ powder was added to the $Ca(OH)_2$ and stirred at 100 rpm for 5 min. The nominal Ga concentrations in the synthesis were 2 wt% (2GaHAp) and 4 wt% (4GaHAp) of the theoretical HAp yield. The sample series is designated according to the nominal Ga concentration. Third, an aqueous solution of 2M H_3PO_4 was added to the starting suspension at an addition rate of 1 mL/min using an automated dosing unit (*TITRONIC® universal, Schott*, Germany) until the pH 6.70 ± 0.05 was reached. The (Ca + Ga)/P molar ratio of the reagents was 1.67 (for pure HAp, Ca/P molar ratio was 1.67). The molar ratio was the same for all the synthesis series. Reaction occurs according to Eq. (2):

$$(10\text{-}x)Ca(OH)_2 + xGa(NO_3)_3 \cdot 9.95H_2O + 6H_3PO_4 \rightarrow Ca_{10\text{-}x}Ga_x(PO_4)_6(OH)_{2\text{-}x}O_x + 3xHNO_3 + (18 + 7.95x)H_2O \tag{2}$$

where $x = 0.3$ (for 2GaHAp), 0.6 (for 4GaHAp), calculated, considering that 2 and 4 wt% are the nominal amount of Ga from the total product yield.

Obtained precipitates were aged in mother liquors at ambient temperature overnight (approximately 20 h). After aging, the precipitates were vacuum-filtered and washed with 1 L of deionized water. Filtered precipitates were dried in an oven at 105 °C for 24 h. Dried precipitates were crushed in a pestle to obtain a fine powder (bioceramic precursor powder). The HAp synthesized without $Ga(NO_3)_3 \cdot 9.95H_2O$ was used as a reference (sample series designated as HAp). To ensure the reproducibility of the syntheses, each composition was synthesized in triplicate.

2.2. Preparation of the bioceramics

To prepare a bioceramic pellet, 0.5 g of the as-synthesized powder was transferred to a cylindrical die of 13 mm diameter and compacted at a uniaxial compression force of 100 MPa for 1 min. The compacted pellets (disks) were sintered at 600, 700, 800, 900, 1000, 1100, and 1200 °C with a heating/cooling rate of 5 °C/min and a holding time of 1 h.

2.3. Physicochemical characterisation

2.3.1. X-ray diffraction analysis

The phase composition of the as-synthesized powders and the heat-treated (600–1200 °C) powders was analyzed using X-ray diffractometry (XRD, *PANalytical*, AERIS, The Netherlands). Before analysis, the heated powders were ground in a mortar to remove aggregates that may have formed due to temperature-induced sintering of the particles. XRD patterns were recorded in a 2θ range from 10 to 70°, with a step size of 0.0435°, using a Ni-filter and Cu Kα radiation at 40 kV and 15 mA.

The quantitative phase composition and Ga substitution in the HAp structure were studied by *Rietveld* refinement with the software *Profex* [33]. Structure models were taken from the ICDD PDF-4+ database version 2023 [34] for hexagonal HAp (PDF# 01-074-0565), monoclinic HAp (PDF# 01-076-0694), and α-TCP (PDF# 04-010-4348). For α-TCP, the scale factor, cell parameters, and crystallite-size-related peak broadening were refined. For HAp, the scale factor, cell parameters, crystallite-size- and micro-strain-related peak broadening, and preferred orientation were refined. The crystallite size was determined from complete refinement of the full pattern using the crystallite size estimation model implemented in *Profex's Rietveld* refinement kernel BGMN [35]. Unit cell volume was calculated using Eq. (3) for the hexagonal structure and Eq. (4) for the monoclinic structure [35]:

$$V = \frac{\sqrt{3}a^2c}{2} \tag{3}$$

where a, c – unit cell parameters

$$V = abc \sin \gamma \tag{4}$$

where a, b, c – unit cell parameters, γ - monoclinic angle.

To locate Ga substitution in the HAp crystal lattice, a complete structure refinement of the 4GaHAp heat-treated at 1100 °C was performed, including refinement of Ca site occupancy factors, fractional coordinates, and thermal displacement parameters. This dataset was selected based on its high Ga substitution and processing temperature,

Table 1

Designation of the sample series, Ga concentration measured using ICP-MS (NM – not measured), and *Rietveld* refinement results of phase composition (errors of phase quantities represent standard deviations of triplicate measurements).

Sample series	Nominal Ga conc., wt %	Measured Ga conc., wt %	Heat treatment temp., °C	HAp, %	α-TCP, %	HAp crystallite size, nm	α-TCP crystallite size, nm
HAp	0	–	as-synthesized	100	0	16.5 ± 1.3 (1,0,0) 47.0 ± 5.5 (0,0,1)	–
		–	800	100	0	77 ± 4	–
		–	900	100	0	100 ± 3	–
		–	1000	99.6 ± 0.5	0.4 ± 0.5	154 ± 15	NM
		–	1100	99.3 ± 0.8	0.7 ± 0.8	247 ± 22	NM
		–	1200	99.2 ± 1.4	0.8 ± 1.4	264 ± 27	NM
2GaHAp	2	1.6 ± 0.1	as-synthesized	100	0	11.0 ± 0.3 (1,0,0) 30.5 ± 0.2 (0,0,1)	–
		NM	800	100	0	37 ± 1	–
		NM	900	90.1 ± 3.3	9.9 ± 3.3	69 ± 2	–
		NM	1000	84.4 ± 1.7	15.6 ± 1.7	85 ± 0	145 ± 17
		NM	1100	80.1 ± 1.5	19.9 ± 1.5	112 ± 6	136 ± 14
		NM	1200	72.3 ± 7.2	27.7 ± 7.2	175 ± 32	148 ± 22
4GaHAp	4	3.3 ± 0.4	as-synthesized	100	0	9.3 ± 0.2 (1,0,0) 25.6 ± 0.3 (0,0,1)	–
		3.6 ± 0.4	800	100	0	32 ± 4	–
		3.6 ± 0.4	900	87.0 ± 5.5	13.0 ± 5.5	62 ± 6	–
		NM	1000	82.1 ± 4.5	17.9 ± 4.5	85 ± 0	145 ± 23
		3.7 ± 0.4	1100	72.8 ± 4.3	27.2 ± 4.3	97 ± 5	122 ± 4
		NM	1200	70.1 ± 7.2	29.9 ± 7.2	150 ± 30	136 ± 25

allowing for a relatively reliable structure refinement. Difference *Fourier* maps of the refined structure were created with the Electron Density Map module in *Profex*.

2.3.2. Inductively coupled plasma mass spectrometry

Inductively coupled plasma mass spectrometry (ICP-MS) (7700X, *Agilent*, USA) was used to measure Ga concentration. The powders were dissolved in deionized H_2O (*Synergy 185, Millipore,* MA, USA) and high-purity HNO_3 (65 %, *ChemLab*, Belgium) solution for at least 20 min at room temperature. Then, suspensions were microwaved at 150 °C for 30 min (heating rate 5 °C/min) to facilitate the complete dissolution of the solid particles. The obtained solutions were cooled and filtered through a filter with a pore size of 12–15 μm to eliminate solid phase impurities.

2.3.3. Fourier transformation infrared spectroscopy

The functional groups of the as-synthesized powders and the heat-treated (600–1200 °C) powders were analyzed using *Fourier* transform infrared spectroscopy (FTIR, *Thermo Fisher Scientific*, USA). Before analysis, the heated powders were ground in a mortar to remove aggregates that may have formed due to temperature-induced sintering of the particles. Spectra were recorded in attenuated total reflectance (ATR) mode. Spectra were obtained at a resolution of 4 cm^{-1} over a range of wavenumbers from 400 cm^{-1} to 4000 cm^{-1}, by co-adding 64 scans. Before every measurement, a background spectrum was taken and subtracted from the sample spectrum.

2.3.4. Thermal analysis

The thermal properties of the as-synthesized powders were determined with thermogravimetric analysis (TGA) (*TGA/DSC 3+, Mettler Toledo,* Switzerland). Approximately 10 mg of the sample was placed into an alumina crucible and heated to 1200 °C at 10 °C/min under an airflow of 10 mL/min.

2.3.5. Scanning electron microscopy and energy dispersive X-ray analysis

The surface morphology of the GaHAp bioceramics pellets was analyzed using a high-resolution field emission scanning electron microscope (*FE-SEM/STEM, Verios 5 UC, Thermo Fisher*). SEM imaging was performed at an accelerating voltage of 2 kV, utilizing through-lens and *Everhart-Thornley* detectors to capture detailed surface features. A low beam current and vector scanning mode were employed to minimize charging effects and potential sample damage, with a dwell time of 50 ns. Before imaging, the samples were coated with a 10 nm carbon layer (calculated for a completely flat Si wafer surface) using a *LEICA EM ACE 200* coater. Other processing of the bioceramics pellet samples was not done. The carbon coating thickness was doubled for energy-dispersive X-ray spectroscopy (EDX) analysis. EDX was performed at 20 kV and 1.6 nA using an *Oxford Instruments X-Max 150* detector.

2.3.6. Density measurement by Archimedes' method and bulk density

The apparent density and open porosity of sintered bioceramics were determined using the *Archimedes* principle and a density determination kit (*YDK 01*, *Sartorius AG*, Germany). First, the samples were weighed and transferred to a vessel for impregnation with water. Then, the vacuum was applied (the air was pumped out from the vessel using a vacuum pump) for 30 min. Samples were poured with water under vacuum and impregnated for 30 min following increased pressure in the chamber, reaching atmospheric pressure. Afterwards, the samples were transferred to the density determination kit and weighed in water and air. The apparent density (d_A) was calculated using Eq. (5):

$$d_A = \frac{m_d{}^* \rho_{liquid}}{m_1 - m_2}, \tag{5}$$

where m_d - a mass of the dry sample (g), ρ_{liquid} - a density of water (g/cm^3), m_1 - a mass of the water-impregnated sample in the air (g), m_2 - a mass of the water-impregnated sample in water (g).

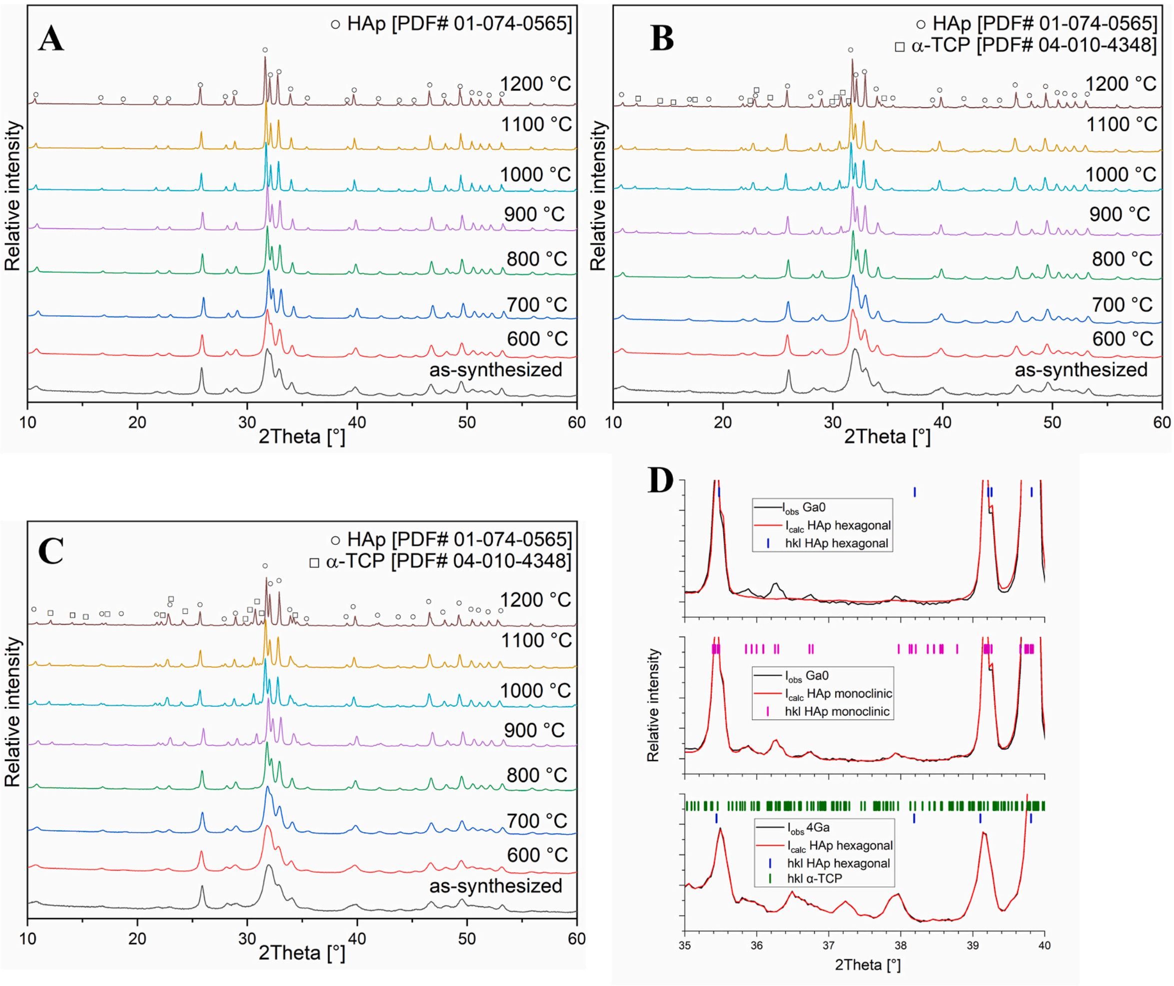

Fig. 1. XRD patterns of the A – Ga-free HAp, B – 2GaHAp, C – 4GaHAp powders heat-treated at temperatures ranging from 600 to 1200 °C, D – XRD patterns at 35–40° 2Theta range of the HAp and 4GaHAp powders heat-treated at 1100 °C, revealing maxima of monoclinic structure (I_{obs} – observed intensity, I_{calc} – calculated intensity).

The open porosity (P_{Op}) was calculated using Eq. (6):

$$P_{Op} = \frac{m_1 - m_d}{m_1 - m_2} * 100, \tag{6}$$

where m_d - the mass of the dry sample (g), m_1 - the mass of the water-impregnated sample in the air (g), m_2 - the mass of the water-impregnated sample in water (g). The bulk density of the green bodies (ρ_0) and sintered bioceramics (ρ) was calculated by dividing the sample mass by its bulk volume (V_{bulk}). The bulk volume was calculated using Eq. (7):

$$V_{bulk} = \frac{\pi d^2 h}{4}, \tag{7}$$

where d and h are the average diameter and height of the sample, respectively, measured using a digital caliper for five samples.

The shrinkage (*Sh*) of the bioceramics after sintering was determined using Eq. (8):

$$Sh = \frac{d_b - d_a}{d_a} * 100, \tag{8}$$

where d_b and d_a are the sample diameters before and after heat treatment, respectively.

3. Results

3.1. Chemical and phase composition

The measured Ga concentrations of the as-synthesized powders are summarized in Table 1. The measured Ga concentrations were close to the theoretically planned or nominal ones. ICP-MS (see 4GaHAp in Table 1) and EDX (Supplementary material, Table S1) analysis confirmed that Ga concentration in the samples does not change after heat treatment.

The phase composition of the HAp and the GaHAp before and after heat treatment at temperatures ranging from 600 to 1200 °C is shown in XRD patterns (Fig. 1(A–C)). Relatively broad and merged XRD diffraction maxima characteristic of the hexagonal HAp phase (PDF# 01-074-0565) indicated low crystallinity of the as-synthesized powders. Furthermore, with increasing Ga concentration, the crystallinity of HAp decreased with temperature increase, as indicated by the broadening of the characteristic XRD diffraction maxima, especially the triplet of (2,1,1), (1,1,2), and (3,0,0) between 30 and 35° 2Theta. The XRD diffraction reveals the formation of a secondary phase that corresponds to the α-TCP phase (PDF# 04-010-4348). In addition, the content of the secondary phase increased with increasing Ga concentration (Fig. 1 (A–C), Table 1).

The crystallite size of HAp is displayed in Table 1. The (0,0,l) diffraction maxima of the as-synthesized powders were less affected by

Table 2

Cell parameters (*a*, *b*, *c*), cell volume (*V*) of HAp and α-TCP, and crystallite size of α-TCP from complete *Rietveld* refinement of full structure (errors represent standard deviations of triplicate measurements).

		HAp				α-TCP			
Heat treatment temp. °C	Sample	*a*, Å	*b*, Å	*c*, Å	Unit cell *V*, Å^3	*a*, Å	*b*, Å	*c*, Å	Unit cell *V*, Å^3
1000	HAp	9.430 ± 0.002	18.775 ± 0.149	6.887 ± 0.002	530.398 ± 0.181	–	–	–	–
	2GaHAp	9.433 ± 0.001	–	6.902 ± 0.002	531.892 ± 0.264	12.890 ± 0.000	27.311 ± 0.002	15.237 ± 0.001	4330.196 ± 0.847
	4GaHap	9.433 ± 0.001	–	6.904 ± 0.002	532.081 ± 0.345	12.8904 ± 0.006	27.311 ± 0.005	15.238 ± 0.001	4330.325 ± 0.808
1100	HAp	9.427 ± 0.001	18.854 ± 0.001	6.886 ± 0.000	529.943 ± 0.047	–	–	–	–
	2GaHAp	9.431 ± 0.002	–	6.907 ± 0.001	532.049 ± 0.376	12.891 ± 0.006	27.306 ± 0.003	15.266 ± 0.005	4337.146 ± 14.606
	4GaHAp	9.431 ± 0.000	–	6.925 ± 0.001	533.387 ± 0.097	12.884 ± 0.000	27.305 ± 0.000	15.231 ± 0.001	4324.93 ± 0.465
1200	HAp	9.427 ± 0.002	18.852 ± 0.002	6.887 ± 0.001	529.956 ± 0.150	–	–	–	–
	2GaHAp	9.430 ± 0.001	–	6.919 ± 0.018	532.812 ± 1.399	12.887 ± 0.005	27.645 ± 0.586	15.231 ± 0.003	4424.457 ± 89.498
	4GaHAp	9.432 ± 0.001	–	6.936 ± 0.007	534.387 ± 0.617	12.886 ± 0.001	27.313 ± 0.004	15.232 ± 0.001	4326.896 ± 0.871

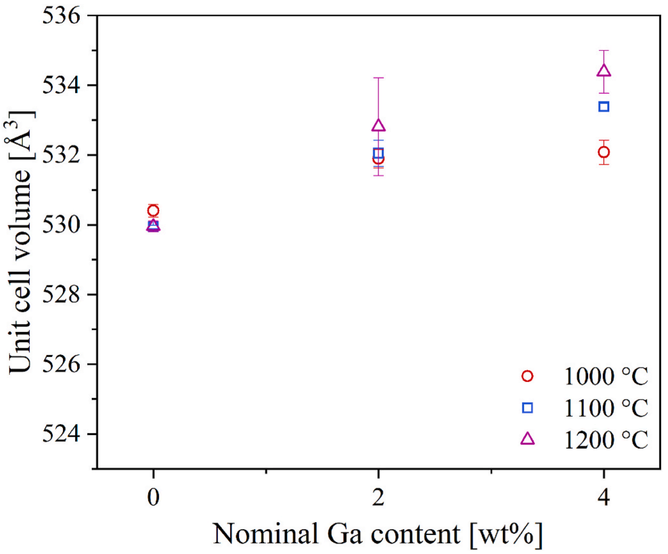

Fig. 2. Refined unit cell volume of the HAp and GaHAp bioceramic heat-treated at 1000, 1100, and 1200 °C as a function of the nominal Ga concentration. The volumes of the monoclinic HAp phase at 0 wt% Ga were divided by 2 to represent a domain equivalent to the hexagonal unit cell.

broadening than all other diffraction maxima, hence requiring refinement of anisotropic crystallite sizes. Datasets of the heat-treated samples were refined with isotropic crystallite sizes. Crystallite size decreased with increasing Ga concentration, and at the highest temperatures (1000–1200 °C), crystallite size was approximately 1.5 times smaller compared to HAp.

Cell parameters (*a*, *b*, *c*), cell volume (*V*) of HAp and α-TCP heat-treated above 1000 °C are displayed in Table 2. In the literature, reported values of hexagonal HAp are $a = b = 9.432$ Å, $c = 6.881$ Å [36], and of monoclinic HAp – $a = 9.4214$ Å, $b = 2a$, $c = 6.8814$ Å [36]. Accordingly, our results showed that the unit cell parameter *c* and the volume of the unit cell of HAp increased with increasing Ga concentration (Fig. 2), suggesting that Ga^{3+} ions were incorporated into the HAp crystal lattice.

The unit cell parameter of α-TCP, shown in Table 2, was not affected by Ga^{3+} substitution and is within the range reported in the literature. Unit cell parameters of α-TCP are reported to be $a = 12.881$ Å, $b = 27.290$ Å, $c = 15.221$ Å by *Stahl* et al. [37], $a = 12.859$ Å, $b = 27.354$ Å, $c = 15.222$ Å by *Tronco* et al. [38], and $a = 12.859$ Å, $b = 27.354$ Å, $c = 15.222$ Å by *Yashima* et al. [39]. The calculated unit cell volume from cell parameters of the α-TCP formed as a secondary phase was higher than reported in the literature, namely, 4310.59 Å3, by *Yashima* et al. [40]. However, it was uncertain to conclude Ga's influence on the α-TCP structure as the phase had a weak diffraction maximum.

3.1.1. Theoretical Ga substitution in the HAp structure

XRD datasets of the HAp heat-treated at 900, 1000, 1100, and 1200 °C showed monoclinic apatite diffraction maxima at 2Theta between 35.5 and 40° (Fig. 1(D)). These additional weak diffraction maxima, indicating a lowering of the symmetry from hexagonal to monoclinic, could not be identified in the XRD datasets of the 2GaHAp and the 4GaHAp heat-treated at the same temperatures, either due to hexagonal symmetry or due to overlap with the secondary α-TCP phase. Hence, a monoclinic HAp structure template was used for *Rietveld* refinement of the HAp datasets. In contrast, the hexagonal structure template was used for all datasets of the 2GaHAp and 4GaHAp at 800–1200 °C, and for the as-synthesized datasets. Structure refinement of the hexagonal HAp phase in the dataset 4GaHAp heat-treated at 1100 °C with a Ga-free hexagonal structure model showed residual unfitted electron densities at the Ca1 position in F_{obs}-F_{calc} *Fourier*

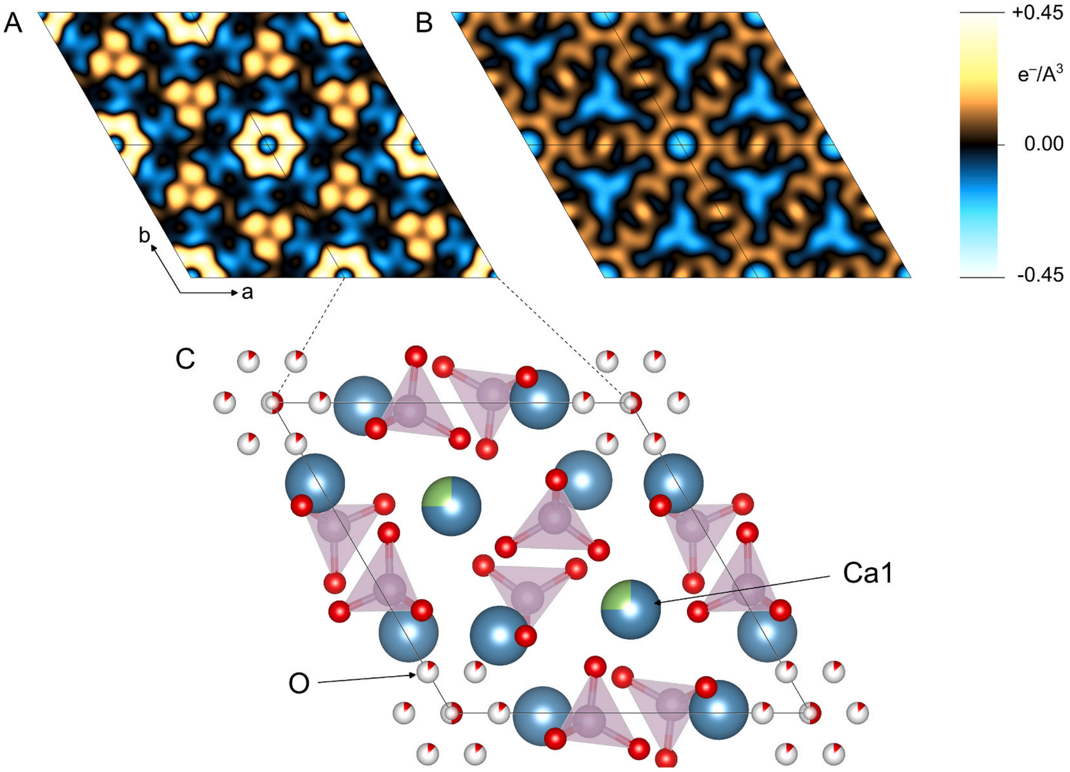

Fig. 3. F_{obs}-F_{calc} *Fourier* synthesis maps at $z = 0.0$ of the 4GaHAp sintered at 1100 °C, refined A – without and B – with the substitution model for Ga. The model is depicted schematically in C. "O" marks the additional oxygen ion compensating the charge imbalance introduced by Ga incorporation on "Ca1".

synthesis maps (Fig. 3(A)). In addition, excess electron densities were also found in the channel along the *c*-axis hosting the OH^- groups (Fig. 3 (A)).

From these signals, we derived a model for the substitution of Ga in the HAp structure. Ga^{3+} ions substitute for Ca^{2+} ions on the Ca1 site, thus introducing an additional positive charge. The charge imbalance is compensated by an additional anion site located in the channel at $x = 0.131$, $y = 0.000$, $z = 0.988$, represented in our refinement model by an additional O^{2-} ion. This uptake of additional ions can explain the unit cell volume expansion in the HAp structure due to the Ga addition. Refining this model with the 4GaHAp heat-treated at 1100 °C reduced residual electron densities in the F_{obs}-F_{calc} *Fourier* synthesis map (Fig. 3 (B)). The substitution model for the hexagonal HAp structure is schematically shown in Fig. 3(C). The refined Ga^{3+} content on the Ca1 site increased with increasing nominal Ga concentration. However, the presence of α-TCP diminished the resolution of the HAp diffraction signal. Hence, the quantification of Ga substitution by *Rietveld* refinement was not considered reliable.

3.2. Functional groups

The functional groups of the HAp and the GaHAp before and after sintering at temperatures ranging from 600 to 1200 °C were analyzed using ATR-FTIR spectra (Fig. 4).

The as-synthesized powders exhibited absorbance bands at 570–580 cm^{-1} attributed to the bending vibrations (ν_4) of PO_4^{3-} and bands centered at 900–1100 cm^{-1} derived from the symmetric and asymmetric stretching vibrations (ν_1 and ν_3) of PO_4^{3-}. Bands at 631 cm^{-1} corresponded to the librational mode (ν_L) of the hydroxyl OH^- groups [41]. Low-intensity absorbance bands were detected at approximately 1418 cm^{-1} and 879 cm^{-1}, attributed to CO_3^{2-} and HPO_4^{2-} groups [42]. The presence of CO_3^{2-} bands was due to a partial carbonation process of the synthesis products, due to the atmospheric CO_2 [43]. Substituting HPO_4^{2-} for PO_4^{3-} acts as a charge compensation mechanism for the cationic deficiency. CO_3^{2-} and HPO_4^{2-} absorbance bands disappeared after heat treatment [42]. The ATR-FTIR data correlated with the XRD data and confirmed the formation of a biphasic mixture of HAp and α-TCP after heat treatment of the 2GaHAp and the 4GaHAp (Fig. 4(B and C)). The difference with heat treatment appeared in the wavenumber region from 900 to 1100 cm^{-1}, where more significant distortion occurred as the heat treatment temperature increased (Fig. 4(A)). The absorbance bands characteristic of the α-TCP phase were detected after heat treatment at temperatures above 800 °C. Namely, the α-TCP PO_4^{3-} groups' absorbance bands at 900–1000 cm^{-1} due to the triple-degenerate asymmetric stretching ν_3, at 940–980 cm^{-1} due to the symmetric stretching ν_1, and at 400–500 cm^{-1} and 550–600 cm^{-1} due to the double and triple-degenerate bending ν_2 and ν_4 [44] were detected as "shoulders" which became more pronounced as the heat treatment temperature increased. In addition, an increase in α-TCP content promoted the decrease of OH^- groups' absorbance at ~3600 cm^{-1}. Moreover, in the case of the 2GaHAp and the 4GaHAp heat-treated above 1000 °C, additional peaks at 502, 734, and 928 cm^{-1} were detected. Their intensity increased with increasing Ga concentration (Fig. 4(D)). Nevertheless, concluding whether new functional groups are created is challenging because various phases and impurities have functional group bands overlapping in the same spectral region. Nonetheless, the presumed peaks might be ascribed to the possible formation of Ga-O bonds. Based on the literature, Ga_2O_3 heat-treated at 1000 °C contains bands (duplicates) in the region 400–850 cm^{-1} [45], and it corresponds to the region of formation of new groups in our study.

3.3. Thermal analysis

Thermal analysis was performed on the as-synthesized HAp, 2GaHAp, and 4GaHAp powders (Fig. 5). The region up to 300 °C corresponds to the dehydration of the samples [46]. The peaks around 50 °C were observed on the DTG curves. According to Refs. [47–49], in the temperature range 50–80 °C, desorption of surface adsorbed water

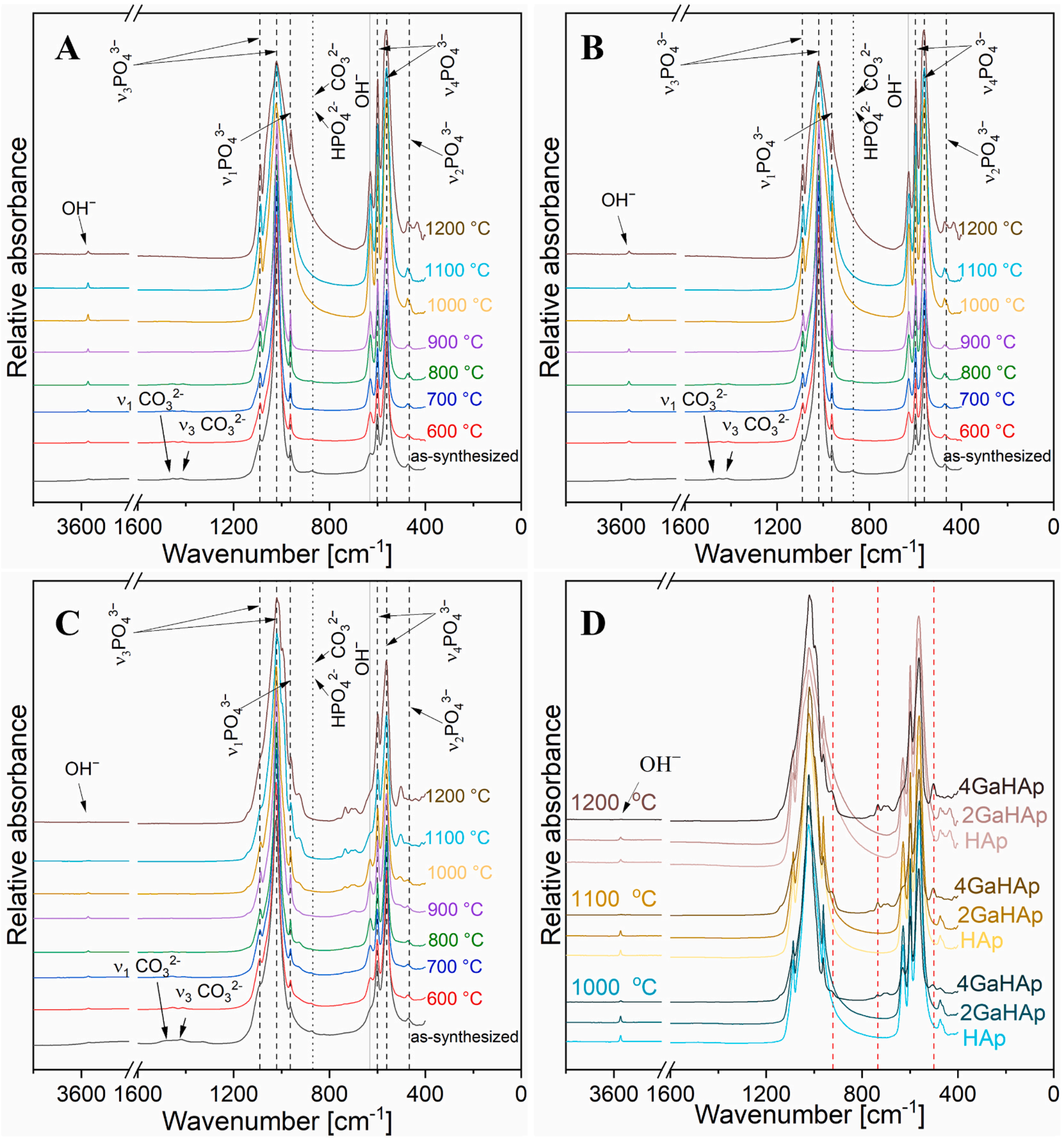

Fig. 4. ATR-FTIR spectra of the A – HAp, B – 2GaHAp, and C – 4GaHAp powders heat-treated at temperatures ranging from 600 to 1200 °C, D – revealing new functional group peaks (marked with red lines) for the samples heat-treated at 1000, 1100, and 1200 °C. (For interpretation of the references to colour in this figure legend, the reader is referred to the Web version of this article.)

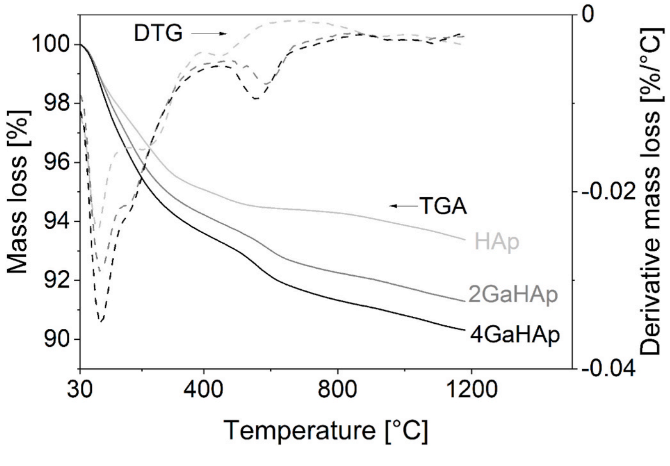

Fig. 5. Thermal analysis of the as-synthesized HAp, 2GaHAp, and 4GaHAp powders.

molecules occurs. In the HAp case, the surface adsorbed water loss resulted in a 1.5 % mass loss, 2GaHAp – 2.1 %, and 4GaHAp – 3.4 %. In turn, the peak shoulder from 80 to 300 °C is related to the water loss from the lattice, chemically bound water inside the pores, or chemisorbed water [50]. This accounted for a mass loss of 3.0 % in the case of HAp, 3.4 % – 2GaHAp, and 3.3 % – 4GaHAp. The temperature region 400–1100 °C corresponds to various thermal events related to crystallization and structural stabilization processes.

According to *Tõnsuaadu* et al., at ~900 °C, dehydroxylation of the HAp phase occurs [46]. The emergence of the additional peak in DTG at ~600 °C for the GaHAp samples can be associated with phase transformation during heat treatment and dihydroxylation that started at a lower temperature. The addition of Ga inhibited crystal growth, leading to the formation of the material with lower crystallinity and promoting the formation of the amorphous phase. It is suggested that at 600 °C, the amorphous part transforms to a more stable CaP. Furthermore, the quantity of the amorphous/low-crystalline phase increased as the Ga content increased, resulting in a higher mass loss of the GaHAp compared to pure HAp. The amorphous phase introduced extra water molecules to the structure due to the presence of a hydrated layer. The

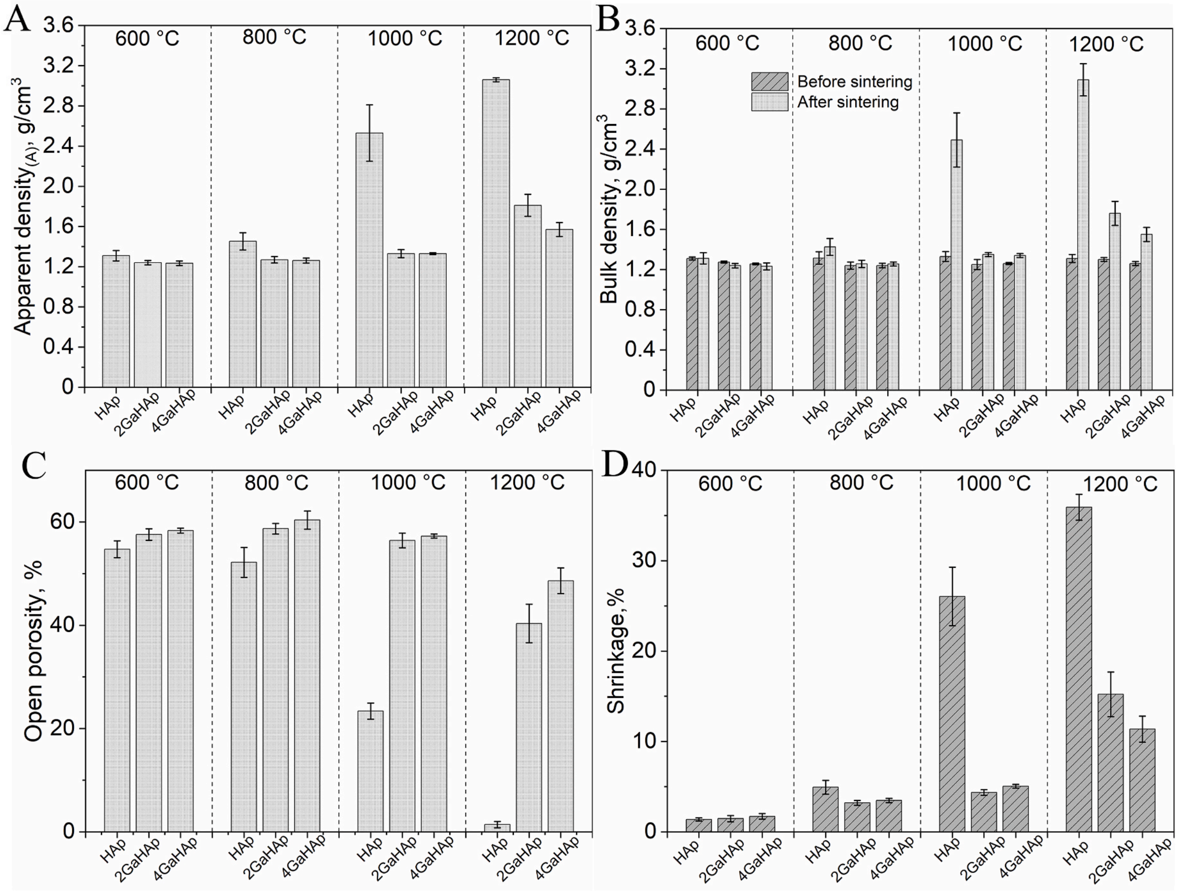

Fig. 6. A – apparent density, B – bulk density, C – open porosity by Archimedes' principle, and D – shrinkage of the HAp and GaHAp bioceramic pellets after sintering at 600 °C, 800 °C, 1000 °C, and 1200 °C.

totals mass loss at 1200 °C for HAp was 6.6 ± 0.4 %, for 2GaHAp – 9.3 ± 0.6 % and for 4GaHAp - 9.8 ± 0.3 %.

3.4. Density

Apparent density, open porosity, shrinkage, and bulk density of the HAp and GaHAp bioceramics sintered at 600, 800, 1000, and 1200 °C were determined and summarized in Fig. 6.

After sintering at 1100 and 1200 °C, the apparent density (Fig. 6(A)) and bulk density (Fig. 6(B)) of the 2GaHAp and 4GaHAp bioceramics were half that of the HAp bioceramics. The open porosity (Fig. 6(C)) was approximately 50 % higher than that of the HAp bioceramics. The shrinkage of the GaHAp bioceramics compared to the HAp was reduced by ~80 % (Fig. 6(D)). The densification process is affected by Ga's impact on crystal growth. Moreover, the formation of a secondary phase in the form of α-TCP significantly decreased densification.

3.5. Microstructure

SEM images confirmed the results of the density measurements, revealing significant differences between the HAp and GaHAp bioceramics microstructures sintered at different temperatures (Fig. 7).

At 600 (Fig. 7(A–C) and 800 °C (Fig. 7(D–F), a substantial difference in microporosity and grain sizes was not observed. Increasing the sintering temperature above 800 °C, *i.e.*, to 1000 °C (Fig. 7(G–I), 1100 °C (Fig. 7(J–L), 1200 °C (Fig. 7(M−O), led to an increase in grain sizes for both the HAp and GaHAp bioceramics. However, Ga promoted the formation of smaller grains and inhibited the densification of HAp regardless of the sintering temperature. As the sintering temperature exceeded 1000 °C, a compact structure consisting of individual hexagonal grains was observed in the case of the HAp bioceramics (Fig. 7(J–M)). At 1100 °C, the 2GaHAp (Fig. 7(K) and 4GaHAp (Fig. 7 (L)) bioceramics had longitudinal-shaped grains. This is associated with grain growth in the *c*-direction. Formation of characteristic hexagonal grains was observed for the GaHAp bioceramics (Fig. 7(N and O) sintered at 1200 °C.

4. Discussion

In the present study, sintering of the GaHAp precursors, *i.e.*, HAp doping with Ga, led to the formation of biphasic CaP bioceramic composed of HAp and α-TCP phases. The refined α-TCP quantities in the Ga-free samples remained below their standard deviations and were thus considered to be below the detection limits. The presence of α-TCP in Ga-doped samples suggests that the Ca/P molar ratio of the synthesis products was less than for stoichiometric HAp, *i.e.*, <1.67. Thus, the syntheses products were CDHAp with chemical formula $Ca_{10\text{-}x\text{-}y}Ga_{x\text{-}y}(HPO_4)_y(PO_4)_{6\text{-}y}(OH)_{2\text{-}x\text{-}y}O_{x\text{-}y}$, where $x = 0.3$ (for 2GaHAp), 0.6 (for 4GaHAp), and $y = 10\text{-}6{*}Ca/P_{\text{experimental}}$. Experimental Ca/P was calculated from the relative proportion of the phases in heat-treated samples following the proposed procedure by *Raynaud* et al. [51]. For example, for the sample 2GaHAp at 1100 °C with a composition of 80.1 % HAp and 19.9 % α-TCP, $y = 0.211$, and 4GaHAp at 1100 °C with a composition of 72.8 % HAp and 27.2 % α-TCP, $y = 0.287$.

The α-TCP formed above 800 °C, and its ratio in the biphasic mixture increased with increasing Ga concentration. According to the literature, the stability of α-TCP is in the range of 1120–1430 °C and up to 1120 °C as a primary phase forms β-TCP, which then transforms to α-TCP [52, 53]. We observed that α-TCP formed at lower temperatures, *i.e.*, at 900 °C. *Martinez* et al. have reported that low-temperature α-TCP

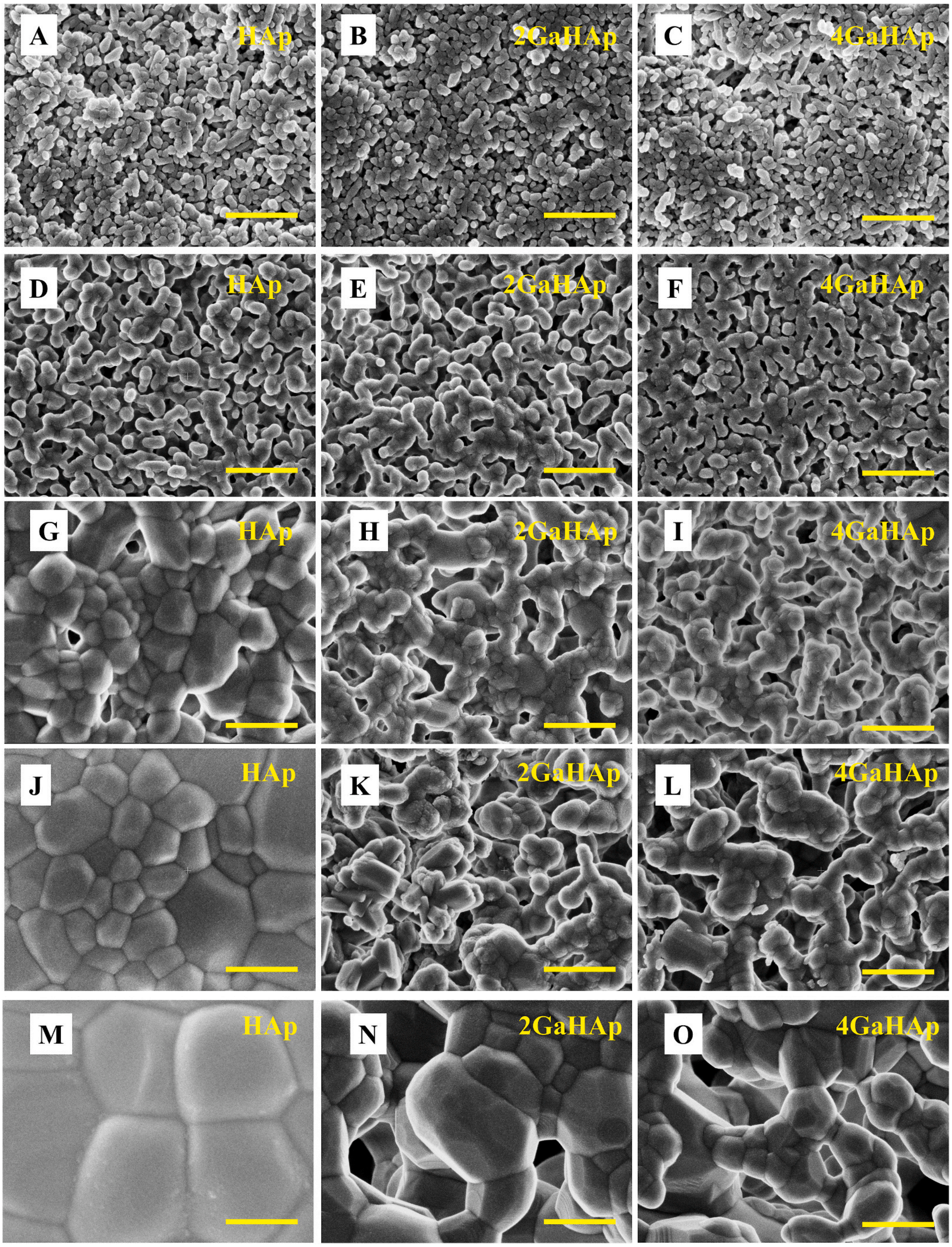

Fig. 7. SEM microphotographs of the A – HAp, B - 2GaHAp, and C – 4GaHAp bioceramic pellets sintered at 600 °C, D – HAp, E – 2GaHAp, F – 4GaHAp bioceramic pellets sintered at 800 °C, G – HAp, H – 2GaHAp, and I – 4GaHAp bioceramic pellets sintered at 1000 °C, J – HAp, K - 2GaHAp, L – 4GaHAp bioceramic pellets sintered at 1100 °C; M – HAp, N – 2GaHAp, and O – 4GaHAp bioceramic pellets sintered at 1200 °C. Scale bar – 500 nm.

(LT-α-TCP) can be obtained at 650 °C from amorphous CaP (ACP) with Ca/P molar ratio of 1.5 [54]. However, they also observed that LT-α-TCP gradually transforms to the β-TCP phase at temperatures above 650 °C. Moreover, *Sinusaite* et al. have suggested that the phase transformations between TCP polymorphs depend on the size and concentration of dopants in the ACP [55]. In our research, both the reduced Ca/P (resulting product is GaCDHAp) and the co-existence of an amorphous phase (reduction in crystallinity due to Ga addition) can promote the development of the α-form. Additionally, a low amount of impurities in the raw material (CaO) can further affect the physicochemical properties, including the thermal stability of CaP phases [56]. It is known that magnesium (Mg) has been shown to stimulate the formation of β-TCP at lower temperatures and increase the β→α transition temperature [46, 55]. As in the present work, the CaO used has a low concentration of Mg, which can also lead to the formation of α-TCP as a secondary phase. Nevertheless, due to the low intensity of secondary phases maxima, it is amiss to evaluate gallium intrusion into the TCP structure. Regarding the Ga effect, the structure refinement of the hexagonal HAp showed Ga incorporation into the Ca1 site in the HAp structure, leading to decreased crystallinity and, thus, disruption of the crystal lattice.

The presence of a secondary phase (TCP) can potentially improve the biodegradability of HAp bioceramics. Namely, the presence of more soluble TCP could enhance the solubility of bioceramics, providing superior ion release and bioactivity [57]. Bioceramics becoming more reactive in biological environments can lead to enhanced formation of a biological apatite on the surface, promoting biomaterial's integration in bone tissues [58].

The observed preference of Ga to enter the HAp lattice structure is consistent with *Zhu* et al.'s proposed explanation that the ions with a smaller ionic radius than Ca tend to occupy the Ca(1) position [59]. Some authors have mentioned that Ga replaces Ca in the HAp lattice structure [60]. However, the specific position of Ga in the HAp crystal lattice was not determined. *Pereira Rocha* et al. proposed that Ga not only replaces Ca but is present in the hydrated or amorphous surface layer of HAp [31]. Poorly crystalline or nanocrystalline HAp was analyzed in the abovementioned studies. Meanwhile, heat-treated HAp was examined in our study, and during sintering, amorphous surface atoms become part of the ordered lattice. Substitution of smaller cations for Ca^{2+} in calcium phosphate phases often leads to a shrinkage of the unit cell volume, as was reported for Mg^{2+} substitution in HAp [61] and β-TCP [62]. In the case of Ga^{3+} substitution, we observed an opposite trend despite the substantially smaller ionic radius of $^{VI}Ga^{3+} = 0.760$ nm versus $^{VI}Ca^{2+} = 1.14$ nm [63]. A similar observation was reported by *Makshakova* et al. for Fe^{3+} substitution in HAp [64]. The unit cell expansion with increasing Ga concentration is most likely related to the incorporation of oxygen ions (O^{2-}) into the channel, replacing the hydroxyl ions (OH^-), to compensate for the additional positive charge introduced by Ga^{3+}.

The addition of Ga significantly influenced the sinterability of the HAp bioceramic at temperatures above 800 °C. According to *Mohammadi* et al., a lower Ca/P molar ratio ($\leq$1.67) resulted in abnormal grain refinement consisting of a few coarse particles surrounded by finer grains. The authors attributed this unusual grain formation to the nucleation and growth of secondary phase crystals and further formations of different CaP phases [65]. In our study, the GaHAp bioceramics exhibited a similar microstructure (Fig. 7). Accordingly, the formation of micropores in the GaHAp bioceramics could be attributed to the formation of biphasic mixtures, where the secondary phase inhibits densification. It is related to the *Zener* pinning, where in the intermediate temperature during heat treatment, CDHAp transforms to the α-TCP and acts as a pinning agent, HAp remains as the matrix, and secondary phase forms dispersed particles at grain boundaries and inhibits grain growth [66]. Thus, in the case of the GaHAp, to obtain a denser bioceramic, higher sintering temperature and longer sintering time are required. This was supported by the increased density of the GaHAp bioceramics sintered at 1200 °C compared to lower temperatures. However, we can benefit from the microporous structure of biphasic GaCaP ceramics. Based on *Trzaskowska* et al. HAp sintered above 900 °C has low porosity, specific surface area (SSA), and bioactivity, and is not biodegradable [57]. Meanwhile, the presence of micropores increases SSA, affecting bioactivity and the ability to absorb liquids and adsorb proteins. The presence of macropores creates a surface essential for cell adhesion, proliferation, and tissue ingrowth [53].

5. Conclusions

The study presents the effect of gallium in a concentration up to 3.3 ± 0.4 wt% on the thermal stability of hydroxyapatite. Gallium affected the properties of the synthesized precursor powders. Hence, the as-synthesized powders contained calcium-deficient hydroxyapatite and amorphous phases, which led to the formation of biphasic calcium phosphates (mixture of hydroxyapatite and α-tricalcium phosphate) during sintering. Thus, doping of hydroxyapatite with gallium affected the phase composition and microstructure of the bioceramic after sintering. The secondary phase, α-tricalcium phosphate, was formed at 900 °C and above, and its content increased with increasing gallium concentration. The formation of the secondary phase during sintering significantly affected the microstructure of the obtained bioceramics. The microporous structure of the gallium-doped bioceramics was observed even at high sintering temperatures. Gallium-doped bioceramics had a density twice as low as that of pure hydroxyapatite bioceramics after sintering at 1200 °C. After sintering at 1200 °C, the porosity of gallium-doped bioceramics was 40.4 ± 3.7 % (2GaHAp) and 48.6 ± 2.5 % (4GaHAp), while for pure hydroxyapatite bioceramics it was only 1.1 ± 0.6 %. From full *Rietveld* refinement, we have created a theoretical substitutional model for gallium-doped hydroxyapatite. Incorporating gallium in the hydroxyapatite lattice occurs in the Ca1 position and introduces an additional positive charge. An additional anion site located in the OH channel is introduced to compensate for charge balance, expanding the hydroxyapatite unit cell volume.

CRediT authorship contribution statement

Marika Sceglova: Writing – review & editing, Writing – original draft, Visualization, Validation, Methodology, Investigation, Formal analysis, Data curation, Conceptualization. **Nicola Döbelin:** Writing – review & editing, Writing – original draft, Software, Resources, Investigation, Formal analysis, Data curation. **Renats Vasiljevs:** Methodology, Investigation, Data curation. **Liga Stipniece:** Writing – review & editing, Writing – original draft, Supervision, Investigation, Funding acquisition, Data curation, Conceptualization. **Janis Locs:** Writing – review & editing, Supervision, Resources, Project administration, Funding acquisition, Data curation.

Declaration of competing interest

The authors declare that they have no known competing financial interests or personal relationships that could have appeared to influence the work reported in this paper.

Acknowledgment

The authors acknowledge financial support for granting Open Access from the European Union's Horizon 2020 research and innovation programme under the grant agreement No. 857287 (BBCE – Baltic Biomaterials Centre of Excellence).

Appendix A. Supplementary data

Supplementary data to this article can be found online at https://doi.org/10.1016/j.ceramint.2025.06.440.

References

[1] E. Champion, Sintering of calcium phosphate bioceramics, Acta Biomater. 9 (2013) 5855–5875, https://doi.org/10.1016/j.actbio.2012.11.029.

[2] D.S. Gomes, A.M.C. Santos, G.A. Neves, R.R. Menezes, C. Grande, C. Grande, A brief review on hydroxyapatite production and use in biomedicine (Uma breve revisão sobre a obtenção de hidroxiapatita e aplicação na biomedicina), Cerâmica 65 (2019) 282–302, https://doi.org/10.1590/0366-69132019653742706.

[3] A. Haider, S. Haider, S.S. Han, I.-K. Kang, Recent advances in the synthesis, functionalization and biomedical applications of hydroxyapatite: a review, RSC Adv. 7 (2017) 7442–7458, https://doi.org/10.1039/C6RA26124H.

[4] D. Anandan, A.K. Jaiswal, Synthesis methods of hydroxyapatite and biomedical applications: an updated review, J. Austr. Ceramic Soc. 60 (2024) 663–679, https://doi.org/10.1007/s41779-023-00943-2.

[5] S. Mondal, S. Park, J. Choi, T.T.H. Vu, V.H.M. Doan, T.T. Vo, B. Lee, J. Oh, Hydroxyapatite: a journey from biomaterials to advanced functional materials, Adv. Colloid Interface Sci. 321 (2023) 103013, https://doi.org/10.1016/j.cis.2023.103013.

[6] X. Wang, S. Huang, Q. Peng, Metal ion-doped hydroxyapatite-based materials for bone defect restoration, Bioengineering 10 (12) (2023) 1367, https://doi.org/10.3390/bioengineering10121367.

[7] A. Noori, M. Hoseinpour, S. Kolivand, N. Lotfibakhshaiesh, S. Ebrahimi-Barough, J. Ai, M. Azami, Exploring the various effects of Cu doping in hydroxyapatite nanoparticle, Sci. Rep. 14, 3421. https://doi.org/10.1038/s41598-024-53704-x.

[8] Y. Li, D. Wang, S. Lim, Fabrication and applications of metal-ion-doped hydroxyapatite nanoparticles, JOJ Mater. Sci. 1 (2) (2017) 555558, https://doi.org/10.19080/JOJMS.2017.01.555559.

[9] K. Pajor, Ł. Pajchel, A. Zgadzaj, U. Piotrowska, J. Kolmas, Modifications of hydroxyapatite by gallium and silver ions—physicochemical characterization, cytotoxicity and antibacterial evaluation, Int. J. Mol. Sci. 21 (2020) 1–15, https://doi.org/10.3390/ijms21145006.

[10] D.-E. Radulescu, O.R. Vasile, E. Andronescu, A. Ficai, Latest research of doped hydroxyapatite for bone tissue engineering, Int. J. Mol. Sci. 24 (17) (2023) 13157, https://doi.org/10.3390/ijms241713157.

[11] S. Sprio, M. Dapporto, L. Preti, E. Mazzoni, M.R. Iaquinta, F. Martini, M. Tognon, N.M. Pugno, E. Restivo, L. Visai, A. Tampieri, Enhancement of the biological and mechanical performances of sintered hydroxyapatite by multiple ions doping, Front. Mater. 7 (2020), https://doi.org/10.3389/fmats.2020.00224.

[12] I. Cacciotti, Cationic and anionic substitutions in hydroxyapatite, in: I.V. Antoniac (Ed.), Handbook of Bioceramics and Biocomposites, Springer International Publishing, Switzerland, 2016, pp. 145–211, https://doi.org/10.1007/978-3-319-12460-5_7.

[13] A. Kurzyk, A. Szwed-Georgiou, J. Pagacz, A. Antosik, P. Tymowicz-Grzyb, A. Gerle, P. Szterner, M. Włodarczyk, P. Płociński, M.M. Urbaniak, K. Rudnicka, M. Biernat, Calcination and ion substitution improve physicochemical and biological properties of nanohydroxyapatite for bone tissue engineering applications, Sci. Rep. 13 (2023) 15384, https://doi.org/10.1038/s41598-023-42271-2.

[14] M. Mosina, I. Kovrlija, L. Stipniece, J. Locs, Gallium containing calcium phosphates: potential antibacterial agents or fictitious truth, Acta Biomater. 150 (2022) 48–57, https://doi.org/10.1016/j.actbio.2022.07.063.

[15] C.R. Chitambar, Gallium-containing anticancer compounds, Future Med. Chem. 4 (2012) 1257–1272, https://doi.org/10.4155/fmc.12.69.

[16] F. Minandri, C. Bonchi, E. Frangipani, F. Imperi, P. Visca, Promises and failures of gallium as an antibacterial agent, Future Microbiol. 9 (2014) 379–397, https://doi.org/10.2217/fmb.14.3.

[17] C.R. Chitambar, Gallium and its competing roles with iron in biological systems, biophys. Acta, Mol. Cell Res. 1863 (8) (2016) 2044–2053, https://doi.org/10.1016/j.bbamcr.2016.04.027.

[18] S.B. Hanaei, R.C. Murugesan, L. Souza, J.I. Cadiz-Miranda, L. Jeys, I.B. Wall, R. A. Martin, Multifunctional gallium doped bioactive glasses: a targeted delivery for antineoplastic agents and tissue repair against osteosarcoma, Biomed. Mater. 19 (6) (2023) 065008, https://doi.org/10.1088/1748-605X/AD76F1.

[19] H. Xi, X. Jiang, S. Xiong, Y. Zhang, J. Zhou, M. Liu, Z. Zhou, C. Zhang, S. Liu, Z. Long, J. Zhou, G. Qian, L. Xiong, 3D-printed gallium-infused scaffolds for osteolysis intervention and bone regeneration, Mater. Today Bio 31 (2025) 101524, https://doi.org/10.1016/j.mtbio.2025.101524.

[20] F. He, J. Rao, W. Fu, J. Zhou, Y. Zhang, T. Chen, W. Huang, Y. Wang, T. Lu, H. Shi, 3D printing and physicochemical and biological characterizations of gallium-containing magnesium/calcium phosphate ceramic scaffolds, Ceram. Int. 49 (21) (2023) 34173–34181, https://doi.org/10.1016/J.CERAMINT.2023.08.127.

[21] C. Mellier, F. Fayon, V. Schnitzler, P. Deniard, M. Allix, S. Quillard, D. Massiot, J. M. Bouler, B. Bujoli, P. Janvier, Characterization and properties of novel gallium-doped calcium phosphate ceramics, Inorg. Chem. 50 (17) (2011) 8252–8260, https://doi.org/10.1021/ic2007777.

[22] M. Shokri, M. Kharaziha, H. Ahmadi Tafti, F. Dalili, R. Mehdinavaz Aghdam, S. R. Ghiassi, M. Baghaban Eslaminejad, Melatonin-loaded mesoporous zinc- and gallium-doped hydroxyapatite nanoparticles to control infection and bone repair, Biomater. Sci. 12 (2024) 4194–4210, https://doi.org/10.1039/D4BM00377B.

[23] W. Shuai, J. Zhou, C. Xia, S. Huang, J. Yang, L. Liu, H. Yang, Gallium-doped hydroxyapatite: shape transformation and osteogenesis activity, Molecules 28 (21) (2023) 7379, https://doi.org/10.3390/molecules28217379.

[24] M. Kurtjak, M. Vukomanović, A. Krajnc, L. Kramer, B. Turk, D. Suvorov, Designing Ga(III)-containing hydroxyapatite with antibacterial activity, RSC Adv. 6 (114) (2016) 112839–112852, https://doi.org/10.1039/c6ra23424k.

[25] M. Kurtjak, M. Vukomanović, D. Suvorov, Antibacterial nanocomposite of functionalized nanogold and gallium-doped hydroxyapatite, Mater. Lett. 193 (2017) 126–129, https://doi.org/10.1016/j.matlet.2017.01.092.

[26] M. Shokri, M. Kharaziha, H.A. Tafti, M.B. Eslaminejad, R.M. Aghdam, Synergic role of zinc and gallium doping in hydroxyapatite nanoparticles to improve osteogenesis and antibacterial activity, Biomater. Adv. 134 (2022) 112684, https://doi.org/10.1016/j.msec.2022.112684.

[27] S. Gokyer, Y.A. Monsef, S. Buyuksungur, J. Schmidt, A.V. Dragomir, S. Uygur, C. Oto, K. Orhan, V. Hasirci, N. Hasirci, P. Yilgor, MgCa-Based alloys modified with Zn- and Ga-Doped CaP coatings lead to controlled degradation and enhanced bone formation in a sheep cranium defect model, ACS Biomater. Sci. Eng. 10 (7) (2024) 4452–4462, https://doi.org/10.1021/acsbiomaterials.4c00358.

[28] N.H. Nguyen, P. Zhang, F.S.P. Kadavan, Z. Xu, T.T. Nguyen, et al., Multifunctional hydroxyapatite coated with gallium liquid metal-based silver nanoparticles for infection prevention and bone regeneration, Adv. Funct. Mater. (2025) 2423496, https://doi.org/10.1002/adfm.202423496.

[29] M. Mosina, C. Siverino, L. Stipniece, A. Sceglovs, R. Vasiljevs, T.F. Moriarty, J. Locs, Gallium-doped hydroxyapatite shows antibacterial activity against Pseudomonas aeruginosa without affecting cell metabolic activity, J. Funct. Biomater. 14 (2) (2023) 51, https://doi.org/10.3390/jfb14020051.

[30] P. Melnikov, A.R. Teixeira, A. Malzac, M.D.B. Coelho, Gallium-containing hydroxyapatite for potential use in orthopedics, Mater. Chem. Phys. 117 (1) (2009) 86–90, https://doi.org/10.1016/j.matchemphys.2009.05.046.

[31] R.L. Pereira Rocha, T.L. Silva, F.P. Araujo, E.G. Vieira, L.M. Honório, M.B. Furtini, M.G. Da Fonseca, E.C. Da Silva-Filho, J.A. Osajima, Gallium-containing hydroxyapatite as a promising material for photocatalytic performance, Minerals 11 (12) (2021) 1347, https://doi.org/10.3390/min11121347.

[32] S. Ponnusamy, R. Subramani, S. Elangomannan, K. Louis, M. Periasamy, G. Dhanaraj, Novel strategy for gallium-substituted Hydroxyapatite/pergularia daemia fiber extract/poly(N-vinylcarbazole) biocomposite coating on titanium for biomedical applications, ACS Omega 6 (35) (2021) 22537–22550, https://doi.org/10.1021/acsomega.1c02186.

[33] N. Doebelin, R. Kleeberg, Profex: a graphical user interface for the rietveld refinement program BGMN, J. Appl. Crystallogr. 48 (5) (2015) 1573–1580, https://doi.org/10.1107/S1600576715014685.

[34] The International Centre for Diffraction Data. https://www.icdd.com, 2024 (accessed 22 October 2024).

[35] J. Bergmann, P. Friedel, R. Kleeberg, BGMN – a New Fundamental Parameters Based Rietveld Program for Laboratory X-Ray Sources, its Use in Quantitative Analysis and Structure Investigations, CPD, 1998, pp. 5–8.

[36] K. Lin, J. Chang, Structure and Properties of Hydroxyapatite for Biomedical Applications, Hydroxyapatite (Hap) for Biomedical Applications, Woodhead Publishing Series in Biomaterials, 2015, pp. 3–19, https://doi.org/10.1016/B978-1-78242-033-0.00001-8.

[37] C. Stähli, A.J. Salinas, N. Döbelin, A. Testino, M. Bohner, Density and phase-purity of α-TCP obtained by sintering of nano-crystalline powder, Ceram. Int. 50 (6) (2024) 8586–8593, https://doi.org/10.1016/J.CERAMINT.2023.07.068.

[38] M.C. Tronco, J.B. Cassel, L.A. dos Santos, α-TCP-based calcium phosphate cements: a critical review, Acta Biomater. 151 (1) (2022) 70–87, https://doi.org/10.1016/j.actbio.2022.08.040.

[39] M. Yashima, A. Sakai, High-temperature neutron powder diffraction study of the structural phase transition between α and α′ phases in tricalcium phosphate $Ca_3(PO_4)_2$, Chem. Phys. Lett. 372 (5–6) (2003) 779–783, https://doi.org/10.1016/S0009-2614(03)00505-0.

[40] M. Yashima, Y. Kawaike, M. Tanaka, Determination of precise unit-cell parameters of the α-Tricalcium phosphate $Ca_3(PO_4)_2$ through high-resolution synchrotron powder diffraction, J. Am. Chem. Soc. 90 (1) (2007) 272–274, https://doi.org/10.1111/J.1551-2916.2006.01375.X.

[41] F. Mohandes, E. Gómez, A. Serrà, Surface modification of hierarchical hydroxyapatite fabricated via hydrothermal method, Ceram. Int. 50 (11-A) (2024) 19283–19292, https://doi.org/10.1016/j.ceramint.2024.03.027.

[42] K. Salma, N. Borodajenko, A. Plata, L. Berzina-Cimdina, A. Stunda, Fourier transform infrared spectra of technologically modified calcium phosphates, IFMBE Proc. 20 (2008) 68–711, https://doi.org/10.1007/978-3-540-69367-3_19.

[43] S. Dey, M. Das, V.K. Balla, Effect of hydroxyapatite particle size, morphology and crystallinity on proliferation of colon cancer HCT116 cells, Mater. Sci. Eng. C 39 (2014) 336–339, https://doi.org/10.1016/J.MSEC.2014.03.022.

[44] M. Motisuke, R.G. Carrodeguas, C.A. de C. Zavaglia, Si-tricalcium phosphate cement: preparation, characterization and bioactivity in SBF, Math. Res. 14 (4) (2011) 493–498, https://doi.org/10.1590/S1516-14392011005000065.

[45] N. Vorobyeva, M. Rumyantseva, V. Platonov, D. Filatova, A. Chizhov, A. Marikutsa, I. Bozhev, A. Gaskov, Ga_2O_3(Sn) oxides for high-temperature gas sensors, Nanomaterials 11 (11) (2021) 2938, https://doi.org/10.3390/nano11112938.

[46] K. Tõnsuaadu, K.A. Gross, L. Plūduma, M. Veiderma, A review on the thermal stability of calcium apatites, J. Therm. Anal. Calorim. 110 (2012) 647–659, https://doi.org/10.1007/s10973-011-1877-y.

[47] D.P. Minh, M.G. Martinez, A. Nzihou, P. Sharrock, Thermal behavior of apatitic calcium phosphates synthesized from calcium carbonate and orthophosphoric acid or potassium dihydrogen orthophosphate, J. Therm. Anal. Calorim. 112 (2013) 1145–1155, https://doi.org/10.1007/s10973-012-2695-6.

[48] M.S. Djošić, V.B. Mišković-Stanković, S. Milonjić, Z.M. Kačarević-Popović, N. Bibić, J. Stojanović, Electrochemical synthesis and characterization of hydroxyapatite powders, Mater. Chem. Phys. 111 (1) (2008) 137–142, https://doi.org/10.1016/j.matchemphys.2008.03.045.

[49] P. Szterner, M. Biernat, Effect of reaction time, heating and stirring rate on the morphology of HAp obtained by hydrothermal synthesis, J. Therm. Anal. Calorim. 147 (2022) 13059–13071, https://doi.org/10.1007/s10973-022-11564-5.

[50] N V Bulina, S V Makarova, S.G. Baev, A.A. Matvienko, K.B. Gerasimov, O. A. Logutenko, V.S. Bystrov, A study of thermal stability of hydroxyapatite, Minerals 11 (12) (2021) 1310, https://doi.org/10.3390/min11121310.

[51] S. Raynaud, E. Champion, D. Bernache-Assollant, J.P. Laval, Determination of calcium/phosphorus atomic ratio of calcium phosphate apatites using X-ray diffractometry, J. Am. Ceram. Soc. 84 (2) (2001) 359–366, https://doi.org/10.1111/J.1151-2916.2001.TB00663.X.

[52] F. He, Y. Tian, Improvements in phase stability and densification of β-tricalcium phosphate bioceramics by strontium-containing phosphate-based glass additive, Ceram. Int. 44 (10) (2018) 11622–11627, https://doi.org/10.1016/j.ceramint.2018.03.236.

[53] J. Liu, L. Zhao, L. Ni, C. Qiao, D. Li, H. Sun, Z. Zhang, The effect of synthetic α-tricalcium phosphate on osteogenic differentiation of rat bone mesenchymal stem cells, Am. J. Transl. Res. 7 (9) (2015) 1588–1601. https://www.ncbi.nlm.nih.gov/pmc/articles/PMC4626420/.

[54] T. Martinez, M. Espanol, C. Charvillat, O. Marsan, M.P. Ginebra, C. Rey, S. Sarda, α-tricalcium phosphate synthesis from amorphous calcium phosphate: structural characterization and hydraulic reactivity, J. Mater. Sci. 56 (2021) 13509–13523, https://doi.org/10.1007/s10853-021-06161-0.

[55] L. Sinusaite, A. Kareiva, A. Zarkov, Thermally induced crystallization and phase evolution of amorphous calcium phosphate substituted with divalent cations having different sizes, Cryst. Growth Des. 21 (2) (2021) 1242–1248, https://doi.org/10.1021/acs.cgd.0c01534.

[56] K. Salma-Ancane, L. Stipniece, Z. Irbe, Effect of biogenic and synthetic starting materials on the structure of hydroxyapatite bioceramics, Ceram. Int. 42 (8) (2016) 9504–9510, https://doi.org/10.1016/J.CERAMINT.2016.03.028.

[57] M. Trzaskowska, V. Vivcharenko, A. Przekora, The impact of hydroxyapatite sintering temperature on its microstructural, mechanical, and biological properties, Int. J. Mol. Sci. 24 (6) (2023) 5083, https://doi.org/10.3390/ijms24065083.

[58] M. Prakasam, J. Locs, K. Salma-Ancane, D. Loca, A. Largeteau, L. Berzina-Cimdina, Fabrication, properties and applications of dense hydroxyapatite: a review, J. Funct. Biomater. 6 (4) (2015) 1099–1140, https://doi.org/10.3390/jfb6041099.

[59] X.D. Zhu, H.J. Zhang, H.S. Fan, W. Li, X.D. Zhang, Effect of phase composition and microstructure of calcium phosphate ceramic particles on protein adsorption, 6, Acta Biomater. 6 (4) (2010) 1536–1541, https://doi.org/10.1016/j.actbio.2009.10.032.

[60] A. Ballardini, M. Montesi, S. Panseri, A. Vandini, P.G. Balboni, A. Tampieri, S. Sprio, New hydroxyapatite nanophases with enhanced osteogenic and anti-bacterial activity, J. Biomed. Mater. Res., Part A 106 (2) (2018) 521–530, https://doi.org/10.1002/jbm.a.36249.

[61] A. Bigi, G. Falini, E. Foresti, M. Gazzano, A. Ripamonti, N. Roveri, Rietveld structure refinements of calcium hydroxylapatite containing magnesium, Acta Crystallogr. B 52 (1996) 87–92, https://doi.org/10.1107/S0108768195008615.

[62] R. Enderle, F. Götz-Neunhoeffer, M. Göbbels, F.A. Müller, P. Greil, Influence of magnesium doping on the phase transformation temperature of β-TCP ceramics examined by rietveld refinement, Biomaterials 26 (17) (2005) 3379–3384, https://doi.org/10.1016/j.biomaterials.2004.09.017.

[63] R.D. Shannon, Revised Effective Ionic Radii and Systematic Studies of Interatomic Distances in Halides and Chalcogenides, vol. 32, 1976, pp. 751–767, https://doi.org/10.1107/S0567739476001551, 5.

[64] O.N. Makshakova, D.V. Shurtakova, A.V. Vakhin, P.O. Grishin, M.R. Gafurov, Incorporation of iron(II) and (III) in hydroxyapatite—A theoretical study, Crystals 11 (10) (2021) 1219, https://doi.org/10.3390/cryst11101219.

[65] M. Mohammadi, J.M. Tulliani, L. Montanaro, P. Palmero, Gelcasting and sintering of hydroxyapatite materials: effect of particle size and Ca/P ratio on microstructural, mechanical and biological properties, J. Eur. Ceram. Soc. 41 (14) (2021) 7301–7310, https://doi.org/10.1016/j.jeurceramsoc.2021.07.025.

[66] D. Fan, L.Q. Chen, S.P.P. Chen, Numerical simulation of zener pinning with growing second-phase particles, J. Am. Ceram. Soc. 81 (3) (1998) 526–532, https://doi.org/10.1111/j.1151-2916.1998.tb02370.x.